IEEE Access
Multidisciplinary | Rapid Review | Open Access Journal

Received March 9, 2020, accepted March 26, 2020, date of publication April 9, 2020, date of current version April 30, 2020.

Digital Object Identifier 10.1109/ACCESS.2020.2986930

Analysis of Thin Truncated Cylinder Scatterers Using Incomplete Hankel Functions and Surface Impedance Boundary Conditions

RENATO CICCHETTI[1], (Senior Member, IEEE), VALENTINA CICCHETTI[1], ANTONIO FARAONE[2], (Senior Member, IEEE), AND ORLANDINO TESTA[1]

[1]Department of Information Engineering, Electronics and Telecommunications, University of Rome "La Sapienza," 00184 Rome, Italy
[2]Advanced Technology, Devices Business, Motorola Solutions, Inc., Fort Lauderdale, FL 33322, USA

Corresponding author: Renato Cicchetti (renato.cicchetti@uniroma1.it)

ABSTRACT The incomplete Hankel functions (IHFs) are employed to evaluate the scattered field from thin truncated cylinders excited by uniform plane waves or by arbitrarily oriented elemental current sources. Metallic and dielectric lossy structures are modeled by means of impedance boundary conditions (IBCs) including surface curvature effects. The scattering currents, expanded in triangular basis functions, are determined upon solving electrical field integral equations (EFIEs) by means of the point-matching method of moments (MoM). The scattered field is then expressed in closed analytical form in terms of IHFs, thus yielding highly accurate numerical results. Furthermore, accurate IHFs approximants are also derived to reduce the computational burden in the analysis of large electrical structures. The proposed approach is demonstrated in practical applications involving cylindrical dielectric structures used in planar lenses, lossy dielectric cylinders suitable to model cane-like vegetation, as well as polarization rotators featuring multiple stages composed of thin metallic wire arrays.

INDEX TERMS Dielectric cylinders, electromagnetic scattering, electrical field integral equations, impedance boundary conditions, IHFs approximants, incomplete Hankel functions, point-matching method of moments, thin wire approximation.

I. INTRODUCTION

Exact analytical solutions of canonical electromagnetic problems yield significant advantages in practical applications, provide physical insights from a theoretical standpoint, and lead to numerically accurate full-wave solvers [1]–[2]. For pulse-shaped and triangular current basis functions commonly employed in the method of moments (MoM) solution of integral equations, the recent introduction of the incomplete Hankel functions (IHFs), whose definitions, properties and analytical approximants can be found in [3]–[4], made it possible to express the fields excited by these canonical basis functions in closed analytical form, further leading to the closed-form computation of MoM reaction integrals [5] thus improving the numerical evaluation of the related field quantities. In particular, in [5], the Galerkin MoM technique was employed to solve an electric field integral equation (EFIE) yielding the scattered field by arrays of thin parallel metal cylinders excited by uniform plane waves, deriving the IHF-based closed analytical form of the MoM impedance matrix coefficients for collinear current basis functions (note that this is not possible for arbitrarily oriented basis function).

Using IHFs and the point-matching MoM technique, electromagnetic scattering from arrays of lossless truncated thin parallel metal wires was analyzed in [4], while a preliminarily investigations on thin parallel dielectric cylinder arrays was presented in [6]. In this paper, the IHFs are further employed to derive the scattered field by finite-length lossy wires and thin dielectric cylinders excited by arbitrary oriented elemental current sources or by uniform plane waves. To this end, a full-wave point-matching MoM approach featuring impedance boundary conditions (IBCs) which take into account the surface curvature is proposed. It is shown that accurate results are obtained in the case of electromagnetic scattering by thin lossy wires, and dielectric cylinders formed by low or high contrast materials. The computation of the MoM matrix coefficients, involving the IHFs integration, is sped up using a novel class of IHF approximants suitable to provide excellent numerical accuracy even for electrically large structures.

The associate editor coordinating the review of this manuscript and approving it for publication was Giovanni Angiulli.

The paper is structured in five sections. Section II describes the MoM approach used for the computation of the field scattered from low and high dielectric contrast thin truncated cylinders modeled by means of IBCs that include surface curvature effects. In Section III, a novel class of highly accurate approximants for the IHFs is introduced and employed in the MoM solution of the related EFIEs. In Section IV, numerical results concerning RF planar lenses, cane-like vegetation on flat soil, and field polarization rotators are presented. Planar RF lenses are useful to increase antenna directivity, propagation processes through vegetation are relevant to radio propagation and remote sensing, while polarization rotators find useful applications in reflector antenna systems [7]–[9]. Concluding remarks are discussed in Section V.

II. ELECTROMAGNETIC SCATTERING MODEL

To describe the focusing effect of electromagnetic lenses formed by thin dielectric cylinders, the field scattered by RF polarization rotators formed by thin lossy wires, as well as the electromagnetic propagation through cane-like vegetation on flat soil, the related EFIEs have been solved by means of a point-matching MoM technique. To model the cylindrical scatterers, surface impedance boundary conditions including curvature effects have been adopted as they provide a reliable model of the physical reality.

The aforementioned applications involve electromagnetic scattering by dielectric or metallic cylinders in free-space, or by dielectric cylinders orthogonal to a lossy half-space. As the latter represents a general case encompassing the others, the proposed approach is described with reference to Fig. 1, where a truncated lossy cylinder, orthogonal to a lossy half-space, is illuminated by the primary field excited by an arbitrarily oriented elemental current source. Image sources are used to model the flat soil [10].

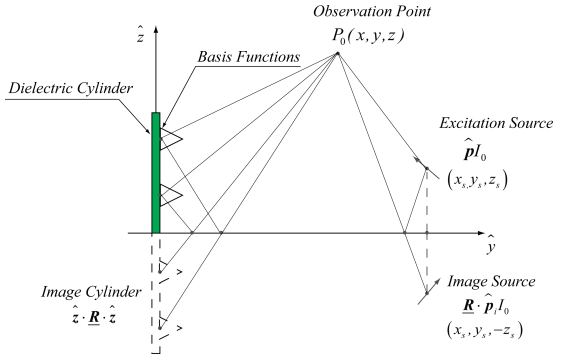

FIGURE 1. Reference geometry: lossy dielectric cylinder placed on a lossy half-space excited by an elemental current source of amplitude I_0 polarized along the $\hat{p}$−direction. The flat soil is modeled using image sources.

The primary field $\boldsymbol{E}^p(\cdot)$ of the elemental current source located at (x_s, y_s, z_s), having amplitude I_0 and polarized along the unit-vector $\hat{\boldsymbol{p}}$, is expressed as

$$\begin{aligned}\boldsymbol{E}^p(x,y,z) = \big[&\underline{\boldsymbol{G}}(x-x_s, y-y_s, z-z_s)\\ &+\underline{\boldsymbol{G}}(x-x_s, y-y_s, z+z_s)\\ &\cdot\underline{\boldsymbol{R}}(x-x_s, y-y_s, z+z_s)\big]\cdot\hat{\boldsymbol{p}}I_0, \end{aligned} \tag{1}$$

where

$$\underline{\boldsymbol{R}} = \left[R_\perp \frac{(\hat{\boldsymbol{s}}\times\hat{\boldsymbol{z}})(\hat{\boldsymbol{s}}\times\hat{\boldsymbol{z}})}{|\hat{\boldsymbol{s}}\times\hat{\boldsymbol{z}}|^2} - R_\parallel\left(\underline{\mathbf{1}} - \frac{(\hat{\boldsymbol{s}}\times\hat{\boldsymbol{z}})(\hat{\boldsymbol{s}}\times\hat{\boldsymbol{z}})}{|\hat{\boldsymbol{s}}\times\hat{\boldsymbol{z}}|^2}\right)\right] \cdot\left(\underline{\mathbf{1}} - 2\hat{\boldsymbol{z}}\hat{\boldsymbol{z}}\right) \tag{2}$$

with

$$R_\perp = \frac{\mu_r\hat{\boldsymbol{s}}\cdot\hat{\boldsymbol{z}} - \sqrt{\varepsilon_r\mu_r - 1 + (\hat{\boldsymbol{s}}\cdot\hat{\boldsymbol{z}})^2}}{\mu_r\hat{\boldsymbol{s}}\cdot\hat{\boldsymbol{z}} + \sqrt{\varepsilon_r\mu_r - 1 + (\hat{\boldsymbol{s}}\cdot\hat{\boldsymbol{z}})^2}}, \tag{3}$$

$$R_\parallel = \frac{\varepsilon_r\hat{\boldsymbol{s}}\cdot\hat{\boldsymbol{z}} - \sqrt{\varepsilon_r\mu_r - 1 + (\hat{\boldsymbol{s}}\cdot\hat{\boldsymbol{z}})^2}}{\varepsilon_r\hat{\boldsymbol{s}}\cdot\hat{\boldsymbol{z}} + \sqrt{\varepsilon_r\mu_r - 1 + (\hat{\boldsymbol{s}}\cdot\hat{\boldsymbol{z}})^2}}. \tag{4}$$

In (1), $\underline{\boldsymbol{G}}(\cdot)$ is the free-space dyadic Green's function [2], $\underline{\boldsymbol{R}}(\cdot)$ is a dyad defining the dependence of the image source on the soil characteristics [10] having defined μ_r and ε_r as the soil complex relative permeability and permittivity. In (2)-(4), $\hat{\boldsymbol{s}}$ is the ray unit-vector joining an image point with the observation point P_0 (see Fig. 1), $\underline{\mathbf{1}}$ is the unit dyadic, while $R_\perp$ and $R_\parallel$ are the Fresnel reflection coefficients for orthogonal and parallel polarization, respectively [1].

Under the thin cylinders hypothesis, the scattered field $\boldsymbol{E}^s(\cdot)$ is expressed in terms of the dominant $z-$polarized current component excited on each of the M cylinders of length l_m and radius a_m ($a_m \ll \lambda_0$) using a triangular basis functions expansion, as follows

$$\begin{aligned}\boldsymbol{E}^s(x,y,z) = \Bigg[\sum_{m=1}^{M}\sum_{n=1}^{N_m}&\boldsymbol{E}_\Lambda(x-x_m, y-y_m, z-z_{mn})\\ &+\boldsymbol{E}_\Lambda(x-x_m, y-y_m, z+z_{mn})\hat{\boldsymbol{z}}\\ &\cdot\underline{\boldsymbol{R}}(x-x_n, y-y_n, z+z_{mn})\cdot\hat{\boldsymbol{z}}\Bigg] I_{mn}\end{aligned} \tag{5}$$

where $\boldsymbol{E}_\Lambda(\cdot)$ is the scattered field generated by a triangular basis function [5], I_{mn} is the weight of the $n-th$ basis function associated to the $m-th$ cylinder whose axis is $\{x = x_m, y = y_m\}$, while z_{mn} establishes its vertical placement.

To determine the current expansion coefficients I_{mn} under the thin cylinders assumption ($a_m \ll \lambda_0$) the following condition, derived from the point-matching application to the curved-surface IBC, is enforced

$$\begin{aligned}&E_z^p(x_m + a_m, y_m, z_{mn}) + E_z^s(x_m + a_m, y_m, z_{mn})\\ &\quad = \frac{Z_{W_m}}{2\pi a_m} I_{mn} \quad m = 1,\cdots,M \; n = 1,\cdots,N_m\end{aligned} \tag{6}$$

where Z_{W_m} is the surface impedance of the $m-th$ cylinder [11], [12]. Straightforward algebra yields the standard MoM matrix form of the EFIE

$$\begin{bmatrix}\underline{\boldsymbol{Z}}_{11} & \underline{\boldsymbol{Z}}_{12} & \cdot & \underline{\boldsymbol{Z}}_{1M}\\ \underline{\boldsymbol{Z}}_{21} & \underline{\boldsymbol{Z}}_{22} & \cdot & \underline{\boldsymbol{Z}}_{2M}\\ \cdot & \cdot & \cdot & \cdot\\ \underline{\boldsymbol{Z}}_{M1} & \underline{\boldsymbol{Z}}_{M2} & \cdot & \underline{\boldsymbol{Z}}_{MM}\end{bmatrix}\cdot\begin{bmatrix}\underline{\boldsymbol{I}}_1\\ \underline{\boldsymbol{I}}_2\\ \cdot\\ \underline{\boldsymbol{I}}_M\end{bmatrix} = \begin{bmatrix}\underline{\boldsymbol{V}}_1\\ \underline{\boldsymbol{V}}_2\\ \cdot\\ \underline{\boldsymbol{V}}_M\end{bmatrix}, \tag{7}$$

where $\underline{\underline{Z}}_{mm}$ is the self-impedance matrix of the $m-th$ cylinder, the matrix $\underline{\underline{Z}}_{mj}$ represents the mutual coupling between $m-th$ and $j-th$ cylinder, while the vector $\underline{V}_m$ consists of the primary field sampled at $(x_m + a_m, y_m, z_{mn})$ with $n = 1, 2, \cdot\cdot, N_m$. Solving (7) yields the current expansion coefficients $\{I_{mn}\}$.

III. THE IHFs ANALYTICAL APPROXIMANTS

The solution of the linear system (7) requires the computation of the $H_0^{(2)}(\Omega, w_0)$ and $H_1^{(2)}(\Omega, w_0)$ *IHFs*−defining integrals [1]. To avoid the numerical computation of these integrals, while maintaining a high level of numerical accuracy, IHFs analytical approximants may be usefully employed. A class of IHFs approximants suitable for analyzing structures having dimensions of the order of a few wavelengths has been introduced in [4]. These approximants are very accurate when the IHFs end-points are in the range $w_0 \in [-5.99, 5.99]$, albeit exhibiting a discontinuity in $w_0 = 0$ that becomes more evident as the IHF argument Ω increases. To illustrate this aspect, the behavior of the relative percentage error caused by the $H_0^{(2)}(\Omega, w_0)$ approximant proposed in [4] for some values of the Ω parameter, when w_0 is proximate to zero, is reported in Fig. 2 and compared with the error produced by the novel approximants derived in the following.

The field excited by triangular current basis functions, appearing in the definition of the MoM impedance matrix coefficients, is expressed in terms of the IHFs $H_0^{(2)}(\Omega, w_0)$ and $H_1^{(2)}(\Omega, w_0)$, whose end-point w_0 depends on the ratio z/ρ (ρ being the radial distance from the axis of the basis function) [5]. For large electrical structures, such as those considered in this paper, w_0 may tend to zero or may assume values outside the range $[-5.99, 5.99]$. Therefore, a new class of IHFs approximants has been developed to overcome the stated limitations of the approximants in [4].

The derivation of these novel approximants is illustrated for the case of the IHF $H_0^{(2)}(\Omega, |w_0|)$, as it may be readily applied to derive the analogous approximant of the IHF $H_1^{(2)}(\Omega, |w_0|)$. The approximant of $H_0^{(2)}(\Omega, |w_0|)$ is obtained starting from the integral representation [4]

$$H_0^{(2)}(\Omega, |w_0|) = -\frac{1}{j\pi} \int_{\cosh w_0}^{\infty} \frac{e^{-j\Omega u}}{\sqrt{u^2-1}}\, du \tag{8}$$

rewritten in the following form

$$\begin{aligned} &H_0^{(2)}(\Omega, |w_0|) \\ &= \left(-\frac{1}{j\pi} \int_1^{\infty} \frac{e^{-j\Omega u}}{\sqrt{u^2-1}}\, du + \frac{1}{j\pi} \int_1^{\cosh w_0} \frac{e^{-j\Omega u}}{\sqrt{u^2-1}}\, du \right) \\ &\quad \times \operatorname{sech}^2 w_0 \\ &\quad + \left(-\frac{1}{j\pi} \int_{\cosh w_0}^{\infty} \frac{e^{-j\Omega u}}{\sqrt{u^2-1}}\, du \right) \left(1 - \operatorname{sech}^2 w_0\right) \end{aligned} \tag{9}$$

where the transition functions $\operatorname{sech}^2 w_0$ and $\left(1 - \operatorname{sech}^2 w_0\right)$ weigh the corresponding terms in (9) which become dominant when w_0 is respectively near or far from $w_0 = 0$. As in [4], the term $1/\sqrt{u^2-1}$ in (9) is rewritten as $1/\left(\sqrt{u-1}\sqrt{u+1}\right)$, then $1/\sqrt{u+1}$ is expanded in terms of exponential functions as follows

$$\frac{1}{\sqrt{u+1}} = \sum_{p=1}^{N} a_p e^{-\alpha_p u} + \varepsilon(u), \tag{10}$$

where a_p and α_p are the expansion coefficients derived through a least square fitting, N is the chosen order of the expansion, while $\varepsilon(u)$ is the approximation error. Straightforward algebra yields the exact expression of the IHF as follows

$$\begin{aligned} H_0^{(2)}(\Omega, |w_0|) = \frac{1}{2} H_0^{(2)}(\Omega) \operatorname{sech}^2 w_0 + \hat{H}_0^{(2)}(\Omega, |w_0|) + \\ -\hat{H}_0^{(2)}(\Omega, 0) \operatorname{sech}^2 w_0 + \tilde{E}_0^{(2)}(\Omega, |w_0|) \end{aligned} \tag{11}$$

with

$$\tilde{E}_0^{(2)}(\Omega, |w_0|) = \hat{E}_0^{(2)}(\Omega, |w_0|) - \hat{E}_0^{(2)}(\Omega, 0) \operatorname{sech}^2 w_0 \tag{12}$$

where $H_0^{(2)}(\Omega)$ is the Hankel function of second kind and order zero [13], $\hat{H}_0^{(2)}(\Omega, |w_0|)$ and $\hat{E}_0^{(2)}(\Omega, |w_0|)$ are the related approximant introduced in [4] and its error, respectively, while $\tilde{E}_0^{(2)}(\Omega, |w_0|)$ is the error introduced by the new proposed approximation. Inserting in (11) the $\hat{H}_0^{(2)}(\Omega, |w_0|)$ expression from [4], and neglecting the error terms (12), the following approximant is obtained

$$\begin{aligned} \tilde{H}_0^{(2)}(\Omega, |w_0|) = \frac{1}{2} H_0^{(2)}(\Omega) \operatorname{sech}^2 w_0 + \frac{e^{-j\Omega}}{j\sqrt{\pi}} \sum_{p=1}^{N} a_p e^{-\alpha_p} \\ \times \frac{\operatorname{sech}^2 w_0 - Erfc\left[\sqrt{(\cosh w_0 - 1)\left(\alpha_p + j\Omega\right)}\right]}{\sqrt{\alpha_p + j\Omega}}. \end{aligned} \tag{13}$$

where $Erfc[\cdot]$ is the complementary error function [13]. Operating analogously, the following approximant for $H_1^{(2)}(\Omega, |w_0|)$ is obtained

$$\begin{aligned} &\tilde{H}_1^{(2)}(\Omega, |w_0|) \\ &= \frac{1}{2} H_1^{(2)}(\Omega) \operatorname{sech}^2 w_0 - \frac{e^{-j\Omega}}{\sqrt{\pi}} \sum_{p=1}^{N} a_p e^{-\alpha_p} \frac{1 + 2\alpha_p + 2j\Omega}{2\sqrt{\left(\alpha_p + j\Omega\right)^3}} \\ &\quad \times \left\{ Erfc\left[\sqrt{(\cosh w_0 - 1)\left(\alpha_p + j\Omega\right)}\right] - \operatorname{sech}^2 w_0 \right\} + \\ &\quad - \frac{e^{-j\Omega \cosh w_0}}{\pi} \sqrt{\cosh w_0 - 1} \sum_{p=1}^{N} a_p \frac{e^{-\alpha_p \cosh w_0}}{\alpha_p + j\Omega}, \end{aligned} \tag{14}$$

whose error depends on the end-point w_0 in a similar fashion as in (12). In (14), $H_1^{(2)}(\Omega)$ is the well-known Hankel function of second kind and order one. The expansion coefficients employed in (13)-(14) are reported in Table 1.

As evinced from (12) the IHF approximants (13)-(14) are characterized by higher numerical accuracy compared to

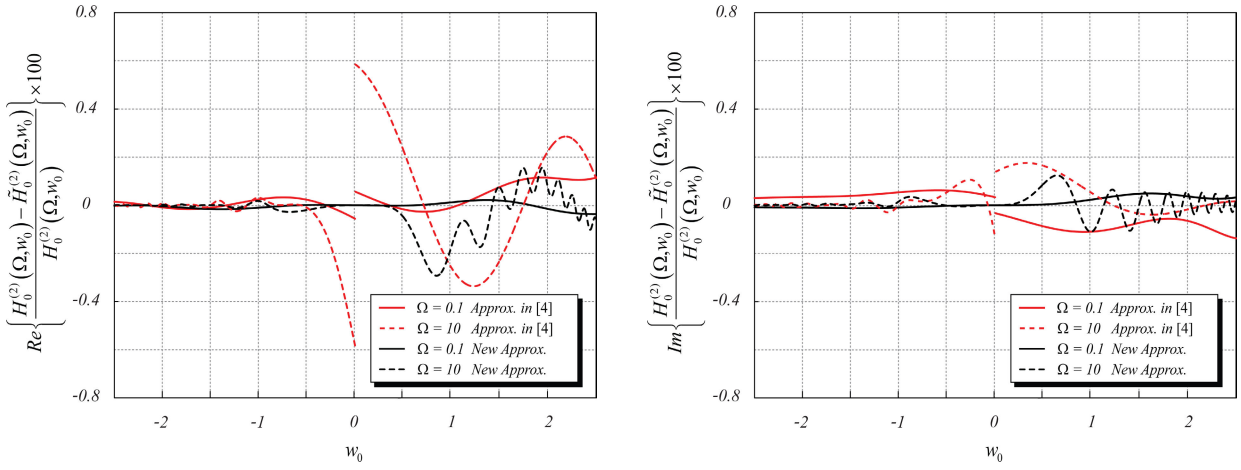

FIGURE 2. Relative percentage approximation error versus w_0 for the approximants of $H_0^{(2)}(\Omega, w_0)$: (a) real part, (b) imaginary part. To better represent the behavior of the errors introduced by the approximants, only the curves corresponding to $\Omega = 0.1$ and $\Omega = 10$ are reported.

TABLE 1. Expansion coefficients for $\tilde{H}_0^{(2)}(\Omega, |w_0|)$ and $\tilde{H}_1^{(2)}(\Omega, |w_0|)$.

$a_1 = 0.28686009$	$\alpha_1 = 0.85326121$
$a_2 = 0.26955590$	$\alpha_2 = 0.24399030$
$a_3 = 0.17305180$	$\alpha_3 = 0.07110396$
$a_4 = 0.10094023$	$\alpha_4 = 0.02037345$
$a_5 = 0.06352352$	$\alpha_5 = 0.00508334$
$a_6 = 0.05044592$	$\alpha_6 = 0.00048272$

those proposed in [4] as their approximation errors vanish for vanishing $|w_0|$ (see Fig. 2 for the $H_0^{(2)}(\Omega, w_0)$ IHF). As observed in [4], the upper validity bound for $|w_0|$ can be made arbitrarily large upon increasing the exponential expansion order N, thereby reducing its error. In fact, the newly proposed approximants exhibit a high numerical accuracy in the expanded end-point range $w_0 \in [-7.5, 7.5]$ when the coefficients reported in Table 1 are used, allowing the accurate and efficient analysis of structures spanning about 20 wavelengths. Moreover, the IHF approximants do not require numerical integration, thus reducing more than five-fold the computational burden compared to the quadrature required by the IHFs defining integrals.

IV. NUMERICAL RESULTS

The proposed approach is employed in the analysis of three distinct applicative examples involving electrically large structures formed by thin wires and dielectric cylinders of finite length. In the first example, the field focusing produced by a composite planar lens consisting of finite, thin parallel dielectric cylinders featuring variable diameter along the lens cross section is analyzed. In the second example the field propagation through cane-like vegetation on flat soil is examined. Finally, in the last example the performance of an RF polarization rotator formed by finite, thin lossy metal wires is investigated. To guarantee high numerical accuracy, 13635 triangular basis functions with a mesh size of about $\lambda_0/34$ are employed in the first example, while about $\lambda_0/20$ was chosen in the last two examples, featuring 24745 and 22339 basis functions, respectively. To compute the spatial distributions of currents and scattered fields, a custom code was developed in the Wolfram Mathematica environment.

A. COMPOSITE PLANAR LENS

The lens, whose geometry is depicted in Fig. 3, is designed to focus RF energy about three wavelengths away from it along the $x-$axis when $z-$polarized plane waves impinge

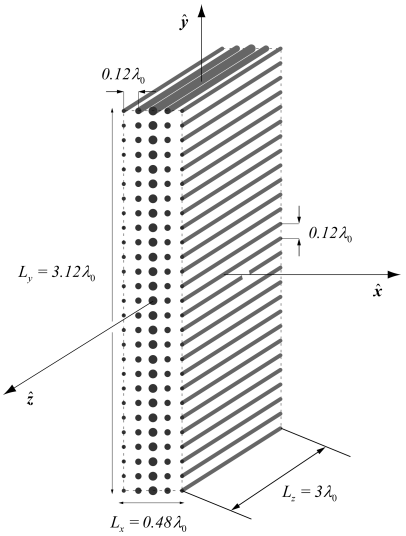

FIGURE 3. Geometry of the planar lens made with 135 thin parallel dielectric cylinders having $\varepsilon_r = 10$. Overall lens size $L_x = 0.48\lambda_0$, $L_y = 3.12\lambda_0$ and $L_z = 3\lambda_0$. The cylinders in the first and last layer have radius $\lambda_0/60$, in the second and in the one before the last layers they have radius $\lambda_0/26$, while in the middle layer they have radius $\lambda_0/20$.

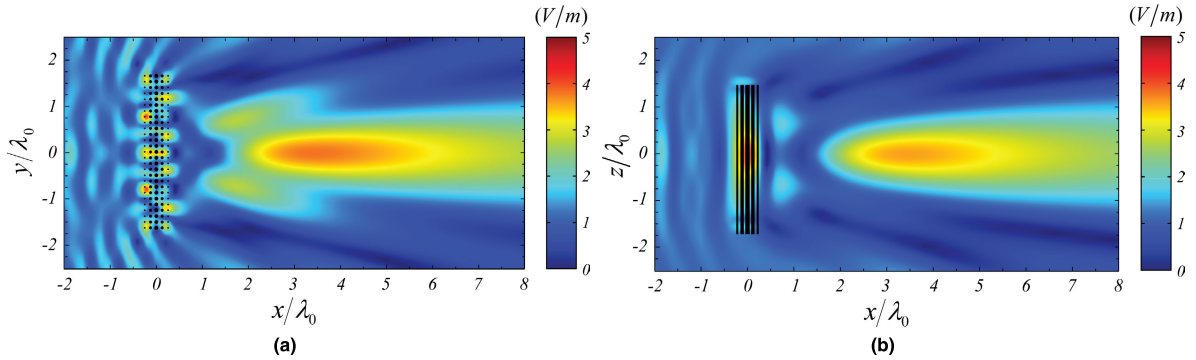

FIGURE 4. Field map of the scattered electric field $z-$component: spatial behavior in the $xy-$plane computed employing the IHF-based approach at $z = 0$ (a), and in the $xz-$plane at $y = 0$ (b). Source characteristics: unit amplitude uniform plane wave polarized along $z-$direction, $f = 5GHz$. The dots in Fig. 4a identify the position of the dielectric cylinders forming the lens.

from the negative $x-$direction. The lens dimensions are $L_x = 0.48\lambda_0$, $L_y = 3.12\lambda_0$ and $L_z = 3\lambda_0$. It consists of 135 thin parallel dielectric cylinders having relative dielectric permittivity $\varepsilon_r = 10$ arranged in air on five parallel planar layers, forming a symmetrical 5×27 uniform square lattice with step $0.12\lambda_0$ in the $xy-$cross section. Focusing is effected upon modulating the effective dielectric constant of the lens through a symmetrical decrease of the cylinders radii, starting from the lens symmetry plane $x = 0$ outward, the chosen radii being $\lambda_0/20$, $\lambda_0/26$, and $\lambda_0/60$. An IBC, which exhibits good electrical characteristics for $\varepsilon_r > 4$ and includes curvature effects [11], was employed to model the thin dielectric cylinders.

The two-dimensional electric field maps presented in Fig. 4 refer to the case of a 1 V/m uniform plane wave at the frequency of 5 GHz normally impinging on the lens, while the $z-$polarized electric field behavior along the $x-$axis is compared with the results obtained using a commercial MoM solver (Altair Feko ^{TM}) in Fig. 5. The scattered field is focused at about three wavelengths from the lens, peaking at about $3V/m$ thereby realizing about $10dB$ focusing gain. Edge diffraction, some limited reflection for $x < 0$, as well as strong electromagnetic coupling between the cylinders forming the lens can be readily observed in Fig. 4. A similar trend between the IHFs based approach and the commercial MoM solver results is observed in Fig. 5.

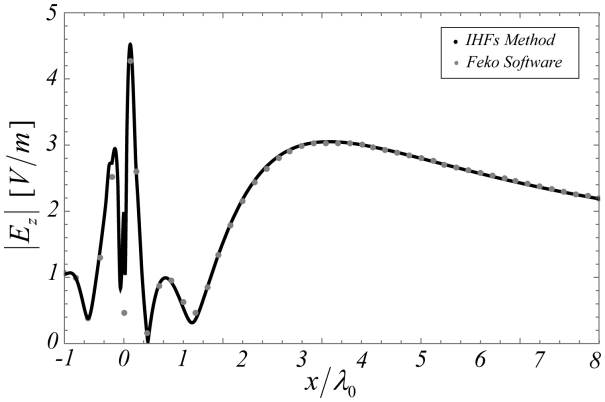

FIGURE 5. Spatial behavior of the scattered electric field $z-$component evaluated along the $x-$direction at $y = 0$ and $z = 0$. Source characteristics: unit amplitude uniform plane wave polarized along $z-$direction, $f = 5GHz$. A similar trend between the IHFs based approach and the full-wave commercial MoM Altair Feko^{TM} solver results can be observed.

B. PROPAGATION THROUGH CANE-LIKE VEGETATION

With reference to Fig. 1, a vertically polarized elemental current source located at $(-10\lambda_0, 0, 2.5\lambda_0)$ is adopted to model an RF emitter operating at $1GHz$ with $1W$ radiated power. The cane thicket, modeled by 245 thin dielectric cylinders (radius $a = 15mm$, length $l = 1.5m$, $\varepsilon_r = 6$, $\sigma_{cyl} = 0.01S/m$) arranged in a regular square lattice (step $\lambda_0/4$) filling an elliptical footprint (axes $x \in [-1.5\lambda_0, 1.5\lambda_0]$, $y \in [-3\lambda_0, 3\lambda_0]$), is placed on flat lossy soil ($\varepsilon_r = 21.5, \sigma = 0.022S/m$). For better adherence with physical reality, an impedance boundary condition including curvature effects was adopted to model the cylindrical scatterers [11].

The two-dimensional map of the electric field $z-$component computed at the source height ($z = 2.5\lambda_0$) is shown in Fig. 6a, while the field map computed in the vertical plane at $y = 0$ is reported in 6b. Finally, the spatial behavior of the vertical electric field computed at $y = 0$, $z = 2.5\lambda_0$ along the $x-$axis is shown in Fig. 7. The strong electromagnetic interference pattern observed within the cane thicket indicates significant interaction between the vegetation and the incident and scattered fields. Concurrently, a focusing process, similar to that observed in a dielectric lens, takes place in the external region beyond the cane thicket, due to the aforementioned interference processes.

C. POLARIZATION ROTATOR

Three parallel, planar rectangular gridded screens, placed at a distance $s = 5mm$ from each other, are formed by arrays of thin parallel lossy copper wires $1mm$ (about $\lambda_0/40$ at $8GHz$) in radius, featuring electrical conductivity $\sigma = 5.96 \times 10^7 S/m$ modelled by means of the IBC proposed in [12]. As in [9], the copper wires are assumed to be in free-space, as if polyurethane foam [9] or similar materials acted as mechanical support.

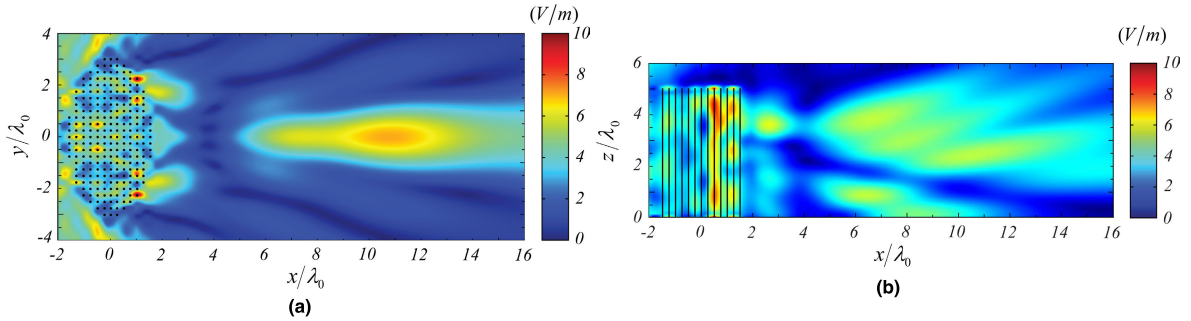

FIGURE 6. Field map of the scattered electric field $z-$component: spatial behavior in the $xy-$plane computed employing the IHF-based approach at $z = 2.5\lambda_0$ (a), and in the $xz-$plane at $y = 0$ (b). Cylinders characteristics: $a = \lambda_0/20$, $l = 5\lambda_0$, $\varepsilon_r = 6$, $\sigma_{cyl} = 0.01\ S/m$ [14]. Source characteristics: $f = 1GHz$, polarization $\hat{p} = \hat{z}$, radiated power $1W$, position $(-10\lambda_0, 0, 2.5\lambda_0)$. Soil characteristics: $\varepsilon_r = 21.5$, $\sigma = 0.022\ S/m$ [15]. The dots in Fig. 6a indicate the position of the 245 dielectric cylinders spaced $\lambda_0/4$ modeling the cane thicket placed on flat soil. A fast spatial variation of field levels within the region where the cane thicket is located, as well as a focusing and reflection (from the soil) process taking place in the external region can be observed in the figures.

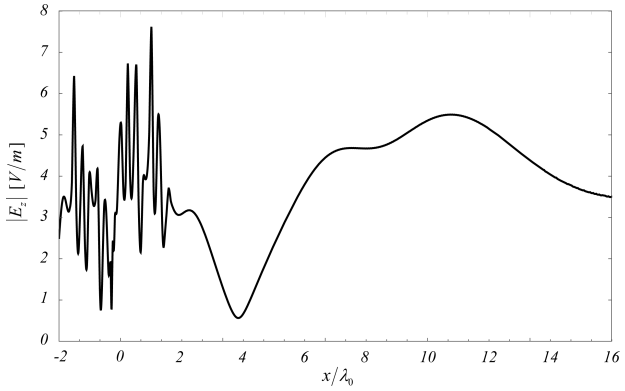

FIGURE 7. Electric field $z-$component evaluated along the $x-$direction. Cylinders characteristics: $a = \lambda_0/20$, $l = 5\lambda_0$, $\varepsilon_r = 6$, $\sigma_{cyl} = 0.01\ S/m$ [14]. Source characteristics: $f = 1GHz$, polarization $\hat{p} = \hat{z}$, radiated power $1W$, position $(-10\lambda_0, 0, 2.5\lambda_0)$. Soil characteristics: $\varepsilon_r = 21.5$, $\sigma = 0.022\ S/m$ [15]. Two field peaks of amplitude $4.7V/m$ and $5.5V/m$ are observed beyond the cane thicket.

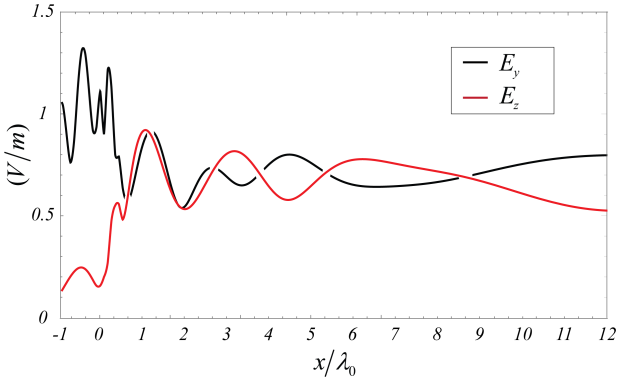

FIGURE 9. Spatial behavior of the magnitude of the $y-$ and $z-$components of the electric field along the $x-$propagation direction at $f = 8GHz$. Geometrical parameters: wire radius $a = 1mm$, distance between layers: $s = 5mm$. In the region next to the rotator ($x = 0$) fast ripples that decay oscillating toward a field component magnitude around $0.7V/m$ can be observed.

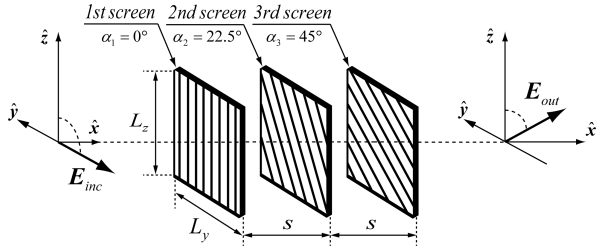

FIGURE 8. Exploded geometry of the polarization rotator composed of three gridded screens formed by thin parallel metal wires. The distance s between the screens is magnified for a better view of the composite structure. The wires rotation angle of each panel is referred to the vertical axis ($z-$axis). Wires array rotation angles: $\alpha_1 = 0°$, $\alpha_2 = 22.5°$, $\alpha_3 = 45°$.

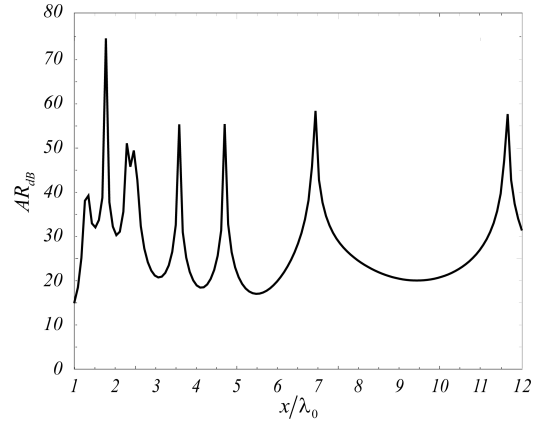

FIGURE 10. Spatial behavior of the axial ratio (AR) along the propagation direction at $f = 8GHz$. Geometrical parameters: wire radius $a = 1mm$, distance between layers: $s = 5mm$. In almost everywhere, the AR remains above $20dB$.

With reference to Fig. 8, the gridded screens dimensions are $L_y = 320mm$, $L_z = 400mm$ and the copper wires are set $10mm$ apart. The wire orientation increases by 22.5° counter-clockwise between screens when looking in the propagation direction of an orthogonally-impinging plane wave, thus targeting about 45° polarization rotation of the outgoing wave.

In this example, a $y-$polarized $1V/m$ uniform plane wave at $8GHz$ impinges orthogonally on the polarizer, which is orthogonal to the $x-$axis and centered at $x = 0$. At this

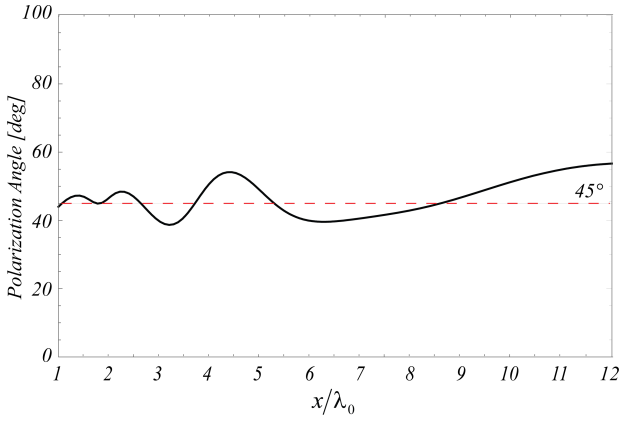

FIGURE 11. Behavior of the electric field polarization angle along the propagation direction at $f = 8GHz$. Geometrical parameters: wire radius $a = 1mm$, distance between layers: $s = 5mm$. The polarization angle fluctuates about 10° with respect to the 45° target value.

operating frequency, each normalized screen electrical dimensions are about $L_y/\lambda_0 = 8.5$, $L_z/\lambda_0 = 10.8$, representing quite an electrically-large structure. The spatial behaviors of the $y-$ and $z-$components of the electric field along the $x-$propagation direction at $y = 0, z = 0$ are shown in Fig. 9, while the behavior of the field axial ratio (AR) is shown in Fig. 10. Finally, the polarization angle of the corresponding emerging electric field is reported in Fig. 11. Fig. 9 shows that the magnitudes of the field components emerging from the rotator ($x > 0$) settle rapidly at about $0.7V/m$, indicating small insertion loss of the rotator. Polarization quality is confirmed by the AR plot in Fig. 10, showing levels above $20dB$ almost everywhere, as well as by observing the limited rotation angle floating around 45° (Fig. 11). Better performances are generally expected for electrically-larger screen sizes and increasing number of cascaded screens [9].

Finally, the 2D field maps in Fig. 12 provide insight into the scattering phenomena governing the polarizer illustrating the co-polar (Fig. 12a) and cross-polar (Fig. 12b) electric field components relative to the 45° target in the plane of the incident electric field. These maps illustrate that the cross-polar component is substantially lower than the co-polar one beyond the rotator, with reduced AR towards the edges of the map due to the rotator lattice and edge diffraction effects.

V. CONCLUSION

An approach based on the Incomplete Hankel functions (IHFs) was proposed for the accurate and efficient evaluation of the scattered field from thin truncated cylinders excited by uniform plane waves or by arbitrarily oriented elemental current sources. Lossy metallic wires and dielectric cylindrical structures exhibiting low or high contrast materials, were modeled using IBCs including surface curvature effects. The scattered fields were computed via the full-wave point-matching method of moments (MoM) based on triangular basis functions, yielding closed form scattered field expressions in terms of the IHFs. Moreover, a new class of analytical IHFs approximants to reduce the MoM computational burden for electrically-large structures were derived. Several examples involving accurate numerical solutions of the scattered fields by composite planar lenses, propagation through cane thickets on lossy soil, and performances attainable by polarizer rotators, were provided to illustrate the broad applicability of the proposed method. Strong coupling effects between cylinders, marked field focusing processes, edge diffraction effects, as well as field reflection from the surfaces forming the analyzed structures were highlighted. Finally, aspects related to the suitable choice of IHFs approximants parameters were discussed.

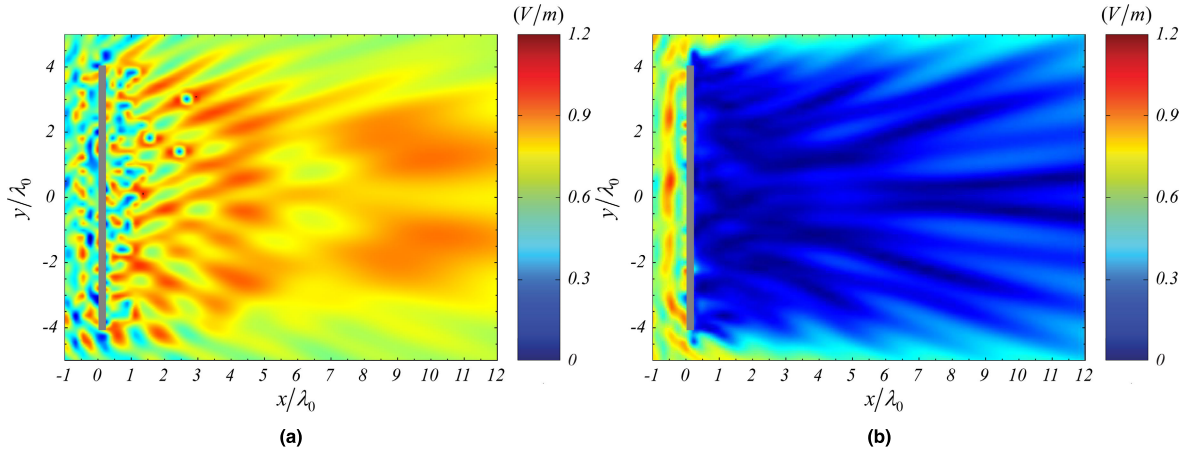

FIGURE 12. Electric field maps computed using the IHF-based approach for the polarization rotator: (a) co-polarized component, (b) crosspolarized component. Rotation angle 45°. Frequency: 8 GHz. Rotator dimensions $L_y = 320mm$, $L_z = 400mm$, wire radius $a = 1mm$, distance between layers: $s = 5mm$. Field amplitude fluctuations caused by diffraction processes taking place in the rotator lattice as well as along the contours of the three screens forming the composite structure are observed in the co-polar field map (a), while the amplitude of the cross polarized component is strongly reduced (b).

REFERENCES

[1] A. C. Balanis, *Advanced Engineering Electromagnetics*. New York, NY, USA: Wiley, 1989.
[2] L. B. Felsen and N. Marcuvitz, *Radiation and Scattering of Waves*. New York, NY, USA: Prentice-Hall, 1994.
[3] R. Cicchetti and A. Faraone, "Incomplete Hankel and modified Bessel functions: A class of special functions for electromagnetics," *IEEE Trans. Antennas Propag.*, vol. 52, no. 12, pp. 3373–3389, Dec. 2004.
[4] R. Cicchetti, A. Faraone, G. Orlandi, and D. Caratelli, "Real-argument incomplete Hankel functions: Accurate and computationally efficient integral representations and their asymptotic approximants," *IEEE Trans. Antennas Propag.*, vol. 63, no. 6, pp. 2751–2756, Jun. 2015.
[5] R. Cicchetti and A. Faraone, "Exact closed-form expression of the electromagnetic field excited by pulse-shaped and triangular line currents," *IEEE Trans. Antennas Propag.*, vol. 56, no. 6, pp. 1706–1716, Jun. 2008.
[6] D. Caratelli, R. Cicchetti, V. Cicchetti, O. Testa, and A. Faraone, "Electromagnetic scattering from truncated thin cylinders: An approach based on the incomplete Hankel functions and surface impedance boundary conditions," in *Proc. Photon. Electromagn. Res. Symp.*, Rome, Italy, Jun. 2019, pp. 1739–1742.
[7] E. Falek and R. Shavit, "A new concept for a flat lens design using dielectric cylinders," *IEEE Trans. Antennas Propag.*, vol. 65, no. 11, pp. 5720–5731, Nov. 2017.
[8] F. T. Ulaby, A. Tavakoli, and B. A. Thomas, "Microwave propagation constant for a vegetation canopy with vertical stalks," *IEEE Trans. Geosci. Remote Sens.*, vols. GE–25, no. 6, pp. 714–725, Nov. 1987.
[9] R. Lech, M. Mazur, and J. Mazur, "Analysis and design of a polarizer rotator system," *IEEE Trans. Antennas Propag.*, vol. 56, no. 3, pp. 844–847, Mar. 2008.
[10] I. Lindell and E. Alanen, "Exact image theory for the Sommerfeld half-space problem, part III: General formulation," *IEEE Trans. Antennas Propag.*, vol. AP-32, no. 10, pp. 1027–1032, Oct. 1984.
[11] J. R. Wait, "Exact surface impedance for a cylindrical conductor," *IEE Electron. Lett.*, vol. 15, no. 20, pp. 659–660, Sep. 1979.
[12] R. Cicchetti and A. Faraone, "Exact surface impedance/admittance boundary conditions for complex geometries: Theory and applications," *IEEE Trans. Antennas Propag.*, vol. 48, no. 2, pp. 223–230, Feb. 2000.
[13] M. Abramowitz and I. A. Stegun, *Handbook of Mathematical Functions*. New York, NY, USA: Dover, 1962.
[14] F. T. Ulaby and R. P. Jedlicka, "Microwave dielectric properties of plant materials," *IEEE Trans. Geosci. Remote Sens.*, vols. GE–22, no. 4, pp. 406–415, Jul. 1984.
[15] P. Hoekstra and A. Delaney, "Dielectric properties of soils at UHF and microwave frequencies," *J. Geophys. Res.*, vol. 79, no. 11, pp. 1699–1708, Apr. 1974.

RENATO CICCHETTI (Senior Member, IEEE) was born in Rieti, Italy, in May 1957. He received the Laurea degree in electronics engineering *(summa cum laude)* from the University of Rome "La Sapienza," Rome, Italy, in 1983. From 1983 to 1986, he was an Antenna Designer at Selenia Spazio S.p.A. (now Thales Alenia Space S.p.A.), Rome, Italy, where he was involved in studies on theoretical and practical aspects of antennas for space application and scattering problems. From 1986 to 1994, he was a Researcher, and from 1994 to 1998, he was an Assistant Professor at the Department of Electronics Engineering, University of Rome "La Sapienza," where he is currently a Full Professor. In 1998, 2002, and 2006, he was Visiting Professor at the Motorola Florida Corporate Electromagnetics Research Laboratory, Fort Lauderdale, FL, USA, where he was involved with antennas for cellular and wireless communications. His current research interests include electromagnetic field theory, asymptotic techniques, electromagnetic compatibility, wireless communications, microwave and millimeter-wave integrated circuits, and antennas. He is a Senior Member of the Institute of Electrical and Electronic Engineers, of the Italian Electromagnetic Society (*SIEm*) and his results listed in Marquis *Who's Who in the World* and *Who's Who in Science and Engineering*. Since 2012, he has been the Lead Editor of the annual special issue on "Wideband, multiband, tunable, and smart antenna systems for mobile and UWB wireless applications" for the *International Journal of Antennas and Propagation*, while currently he is one of the coordinators of the research project "Ultra-wideband virtual imaging extra wall for high-penetration high quality imagery of enclosed structures" (U-VIEW) funded by the Italian Ministry of Education, University and Research (MIUR).

VALENTINA CICCHETTI was born in Isernia, Italy, in 1993. She received the master's degree *(cum laude)* in electronics engineering from the Sapienza University of Rome, in 2018, where she is currently pursuing the Ph.D. degree in information and communications technology. Her research interests include applied electromagnetics, wideband and ultrawideband antenna systems, and the analysis of the related electromagnetic compatibility problems.

ANTONIO FARAONE (Senior Member, IEEE) was born in Rome, Italy, in 1966. He received the Ph.D. in applied electromagnetics from the University of Rome "La Sapienza," in 1997. He joined Motorola (now Motorola Solutions Inc.) Corporate Electromagnetic Energy (EME) Research Laboratory, Fort Lauderdale, FL, USA, engaging in mobile antenna technology and RF dosimetry research, as well as the IEEE and IEC RF exposure safety and product compliance standards. At Motorola Solutions, he serves as the Chief EME Scientist, overseeing product RF exposure compliance, is a Scientific Advisory Board Associates (SABA) Member, a Master Innovator, and a Dan Noble Fellow. He has coauthored 37 refereed journal publications and holds 39 patents, mostly on antenna technologies. He currently holds the chairs of Board of Directors of the Mobile & Wireless Forum, an international industry association supporting research into RF health and safety and promoting wireless device integrity and accessibility.

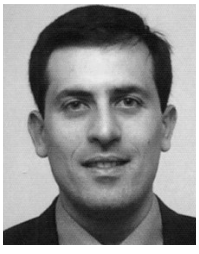

ORLANDINO TESTA was born in Minturno, Italy, in August 1972. He received the Laurea degree *(cum laude)* in electronic engineering and the Ph.D. degree from the University of Rome "La Sapienza," Rome, Italy, in 1997 and 2003, respectively. Since 2001, he has been a High School Teacher at the I.T.I.S. "G. Armellini" Institute of Rome, where he is involved in teaching electronics and telecommunications. He is currently collaborating with the Department of Electronic Engineering, University of Rome "La Sapienza." He is studying high-frequency models for the analysis of radio coverage in indoor environments and tunnels with particular attention to EMC/EMI problems. His main research interests are propagation and radiation of electromagnetic fields, electromagnetic compatibility, microwave and millimeter-wave integrated circuits, and antennas.